pubs.acs.org/journal/apchd5

Article

Lithographically Defined Zerogap Strain Sensors

Published as part of ACS Photonics virtual special issue "Frontiers and Applications of Plasmonics and Nanophotonics".

Mahsa Haddadi Moghaddam, Daryll J. C Dalayoan, Daehwan Park, Zhihao Wang, Hwanhee Kim, Sunghoon Im, Kyungbin Ji, Daeshik Kang, Bamadev Das,* and Dai Sik Kim*

Cite This: *ACS Photonics* 2024, 11, 3239−3249

Read Online

ACCESS | Metrics & More | Article Recommendations | SI Supporting Information

ABSTRACT: Metal thin films on soft polymers provide a unique opportunity for resistance-based strain sensors. A mechanical mismatch between the conductive film and the flexible substrate causes cracks to open and close, changing the electrical resistance as a function of strain. However, the very randomness of the formation, shape, length, orientation, and distance between adjacent cracks limits the sensing range as well as repeatability. Herein, we present a breakthrough: the Zerogap strain sensor (ZSS), whereby lithography eliminates the randomness and violent tearing process inherent in conventional crack sensors and allows for short periodicity between gaps with gentle sidewall contacts, critical in high strain sensing enabling operation over an unprecedentedly wide range. Our sensor achieves a gauge factor of over 15,000 at an external strain of ε_{ext} = 18%, the highest known value. With the uniform gaps of four-to-ten thousand nanometer widths characterized by periodicity and strain, this approach has far reaching implications for future strain sensors whose range is limited only by that of the flexible substrate, with non-violent operations that always remain below the tensile limit of the metal.

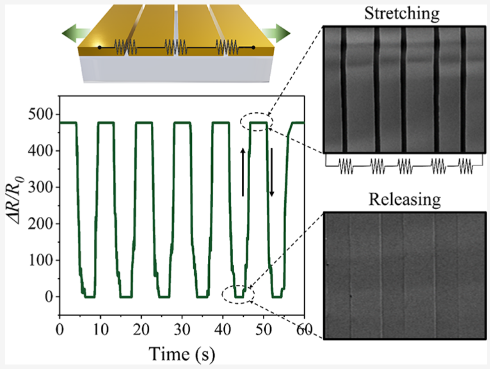

KEYWORDS: *Zerogap, metal thin film, strain sensors, gauge factor, crack sensors*

■ INTRODUCTION

Stretchable strain sensors capable of converting large mechanical deformation into electrical signals are promising candidates for soft and flexible devices, such as skin-mounted electronics,[1−6] wearable health devices,[7−11] and soft robotics.[7,8] Most stretchable strain sensors use advanced composite materials, such as carbon nanotubes,[12−15] graphene and its derivatives,[16−20] nanofibers,[21−25] nanoparticles,[26−28] and metal thin films.[29−37] Recent studies reveal that the formation of spontaneous cracks in metal thin films on soft polymers, triggered by mechanical mismatch with the underlying substrates, enables high-performance crack-based strain sensors.[29,31−33]

Clearly, precise nanocrack patterning techniques are crucial for their practical application. Studies have shown that the pattern of nanocracks significantly impacts the performance of highly sensitive strain sensors.[33−35] Excessive tensile stress creates cracks in the metal film that lead to the formation of nanocracks. This occurs primarily through direct bending or stretching of flexible polymer substrates, a widely used method in the production of nanocracks. However, it is a great challenge to precisely control the pattern of nanocracks, such as the crack position, density, length, and shape, since cracks always tend to randomly arise from intrinsic defects of the film when directly bent or stretched. The randomness of nanocrack patterns degrades the reproducibility of nanocrack-based devices and limits the mass production and practical applications of nanodevices.

To alleviate the inherent randomness of the crack process, efforts to partially orient the cracks perpendicular to the strain direction resulted in higher gauge factors but still the sensing range remains below 5%.[29,31,32] This is mainly due to the average distance between cracks being in the 100 μm range limited by the material properties, which makes the gap opening too fast as a function of the strain, reaching the infinite resistance prematurely. What we need is a lithographically defined, controllable nanometer-to-micrometer gap opening without having gone-through the tearing process inherent in any cracking,[38−41] while maintaining noninfinite resistance at high strain with reasonable gauge factors with desired scalability and consistency of the final samples.

Received: April 3, 2024
Revised: June 25, 2024
Accepted: June 26, 2024
Published: July 15, 2024

https://doi.org/10.1021/acsphotonics.4c00627
ACS Photonics 2024, 11, 3239−3249

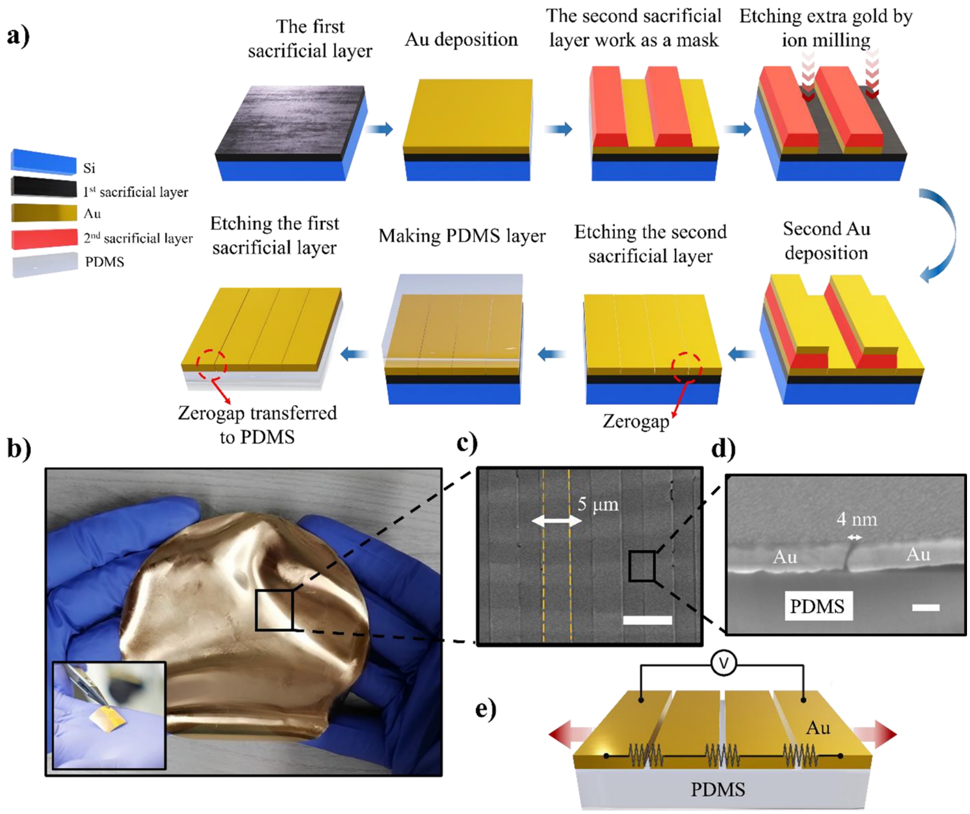

Figure 1. Zerogap strain sensor (ZSS) fabrication. (a) Schematic diagram of the fabrication process and transfer of the Zerogap embedded in micrometer periodicity to the flexible substrate. (b) Photograph of the wafer scale 5ZSS (inset shows a 2 cm by 2 cm ZSS used in experiments). FE-SEM images of the (c) top view and (d) cross-sectional view of a fabricated 5ZSS after transfer to the PDMS substrate before application of the strain (scale bars are 10 μm and 50 nm, respectively). (e) Schematic representation of the sensing mechanism of ZSS: changing resistance by stretching.

In this paper, we present an advanced stretchable crack-based sensor without the conventional cracking process, a Zerogap[42,43] strain sensor (ZSS) where 3–5 nm-wide gaps in the electrical contact are formed along the lithographically arranged periodic lines, which then widen with increasing strain resulting in increased electrical resistance. Our ZSS offers remarkable advances over previous methods, removing extreme forces involved in the tearing process, enabling any short period required for the high strain sensing, limited only by the lithography machine and not by the material characteristics. This is possible by transferring Zerogap samples grown on rigid substrate onto polydimethylsiloxane (PDMS). Employing this technology, we studied the sensitivity of ZSS sensors by changing periodicities from 5 to 500 μm. The characterization of the samples indicates a linear correlation between the periodicity and the gap widening under external stress. Thanks to this property, our sensor with a periodic gap of 5 μm (5ZSS) can operate over a wide strain range and exhibits an extremely high gauge factor of 15,000 at an external strain of 13%< ε_{ext} < 18%, which is due to the presence of regularly arranged long and dense parallel gaps. This wide strain coverage and high range of resistance gauge factors is unprecedented for metal-based crack sensor, where the application is limited to either low[29,31,32] or high[44,45] strain range. In contrast, our ZSS has proven remarkably effective over a diverse span of applications such as pressure sensors, biomechanical dynamics, face recognition, and human body movement. In addition, the proposed strain sensor shows a dynamic response of 10 Hz or more, faster than modulation reported before.[29,31,32]

RESULTS AND DISCUSSION

Structure Design and Characterization. Figure 1a illustrates the detailed fabrication scheme as follows: the first sacrificial layer (here, vanadium 120 nm) and a bare gold (Au) film with a thickness of 50 nm are evaporated onto a rigid substrate (Silicon). Microscale arrays (the second sacrificial layer) are patterned on the Au layer by using standard photolithography as a mask for the ion milling process. After the exposed part of the Au film is etched, a second Au layer with the same thickness is deposited on the entire structure. To ensure good bonding, a 3 nm-thick adhesive layer of titanium (Ti) was deposited immediately before both the first and second Au layers were deposited. Chemical etching of the photoresist creates periodic arrays with a lateral Zerogap between the two Au layers, which are gently connected. PDMS is spin-coated onto the well-aligned Zerogaps and then cured to form a thin and uniform elastomeric film (with a thickness of about 450 μm). In order to achieve superior performance, stretchability, and cyclic stability, 3-mercaptopropyl trimethoxysilane (MPTMS) is used as a precursor between Au patterns and the PDMS layer. It should be noted that the self-assembling MPTMS monolayer can enhance the adhesive interaction of PDMS with the Au patterns. Finally, the Zerogap-patterned Au film is separated from the rigid substrate by chemical etching of the first sacrificial layer and transferred to the elastomer substrate. Figure 1b shows a wafer-scale ZSS

https://doi.org/10.1021/acsphotonics.4c00627
ACS Photonics 2024, 11, 3239−3249

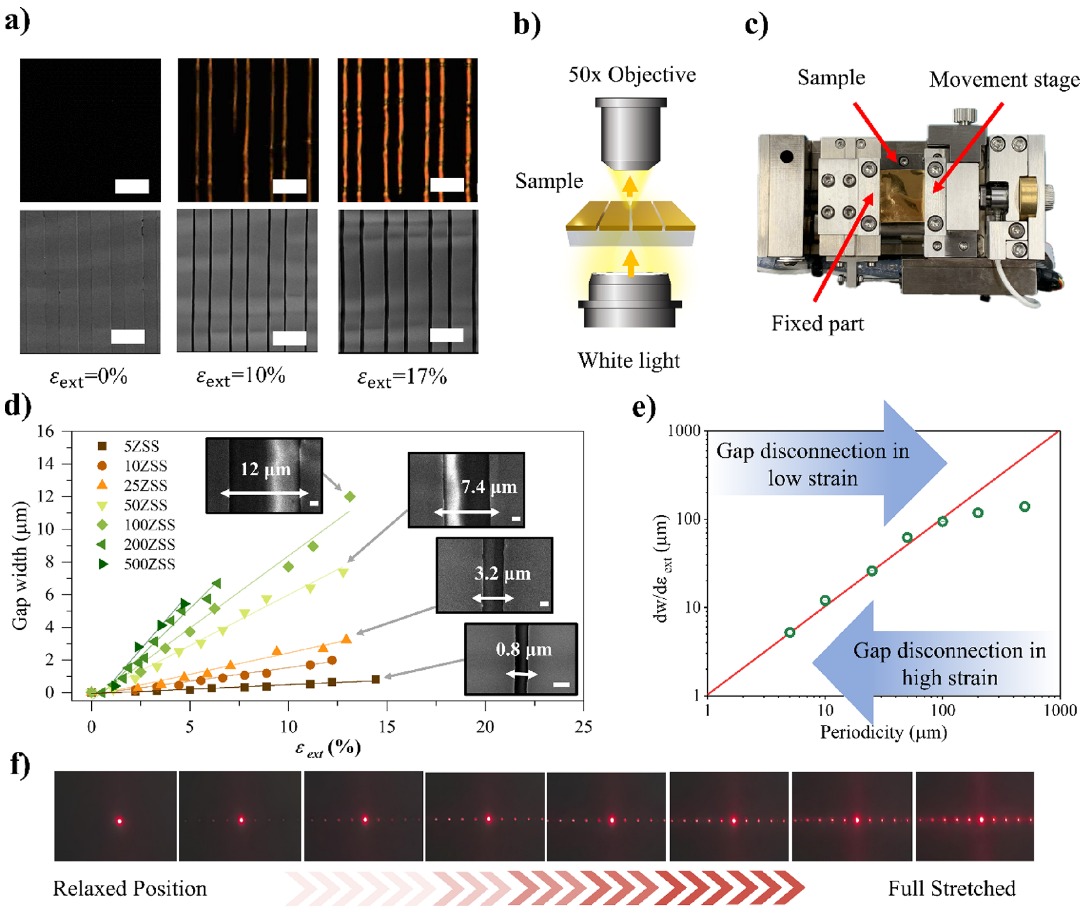

Figure 2. Characterization of the ZSS. (a) Optical transmission (top) and FE-SEM images (bottom) of 5ZSS at ε_{ext} = 0, 10, and 17% (scale bars 10 μm). (b) Schematic diagram illustrating the optical microscope setup used to analyze the transmission of the 5ZSS. (c) Photograph of the in situ tensile stage used in FE-SEM setup. (d) Gap width as a function of external strain for different periodicities measured by FE-SEM images. (Solid lines are linear fitting for each periodicity. The gap width exhibits a linear response throughout the whole strain range.) The insets show the single gap opening at different periodicities around 13% external strain (scale bars 1 μm). (e) Rate of change of the gap under external strain for different periodicities (the solid red line shows a linear fit with a slope of 1, and both axes are in log scale). (f) Diffraction patterns for a 50 μm periodicity 50ZSS sample illuminated by a helium neon laser with 633 nm wavelength from the relaxed position to 20% strain.

with a periodicity of 5 μm (5ZSS), and the inset is a typical 2 cm × 2 cm sample used for the characterization experiments. A field emission scanning electron microscopy (FE-SEM) image of the 5ZSS after transfer to PDMS in the unstretched position is shown in Figure 1c. The cross-sectional image of FE-SEM (Figure 1d) shows that although the two layers are perfectly connected in terms of both electrical and optical functions, they are in fact separated by 4 nm on average. The diagram in Figure 1e illustrates that the resistors are connected in series between parallel slits. An external strain perpendicular to the parallel slits which is defined as $\varepsilon_{ext} = (L - L_0)/L_0 \times 100(\%)$ (L and L_0 are the stretched and relaxed length of the sample, respectively) caused the separation between two adjacent gold bars, which led to an expansion of the gaps from nanometer to micrometer scale and caused a change in resistance. For 5ZSS, the gap opening is visually confirmed by optical transmission images (Figure 2a, top) under an optical microscope (Figure 2b) and FE-SEM images (Figure 2a, bottom) using an in situ tensile stage (Figure 2c) at three different ε_{ext}, namely, relaxed (0%), medium (10%), and fully stretched (17%) (see further details of the gap opening in Figure S1 in the Supporting Information). The robust adhesion of the Au film to the PDMS substrate enables stable strain without delamination of the thin film. Figure 2d, which illustrates the gap opening under external strain measured by FE-SEM for different periodicities, shows perfect linearity for a smaller period ($p \leq$ 50 μm) according to $w = p\varepsilon_{ext}$, where w is the gap width and p is the periodicity. At a larger p, the linearity with ε_{ext} is still maintained. The insets provide FE-SEM images of gap opening around 13% strain for periodicities of 5 (5ZSS), 25 (25ZSS), 50 (50ZSS), and 100 μm (100ZSS). With an identical external strain, the gap width in samples with lower density (w = 12 μm for 100ZSS) is notably larger compared with samples with higher density (w = 0.8 μm for 5ZSS), which corresponds to a 15-fold difference but smaller than (100 μm)/(5 μm) = 20. This deviation from the perfect linearity (red line) is more apparent in Figure 2e for 100ZSS, 200ZSS (p = 200 μm), and 500ZSS (p = 500 μm). In cases where all gaps are uniformly elongated and parallel, samples with a higher gap density require more energy to separate the gap junctions to a set separation where the resistive contact is completely lost. Most of the stress is concentrated at the periodic junctions as long as the gold bars remain crack-free which applies to the small p regime (Figure S2a−c in the Supporting Information). However, at larger p > 100 μm, inherent cracks emerge in the Au film, which effectively makes the p smaller leading to a deviation from the perfect linear line. The formation of uncontrolled cracks in large periodicities from 200 to 500 μm

https://doi.org/10.1021/acsphotonics.4c00627
ACS Photonics 2024, 11, 3239−3249

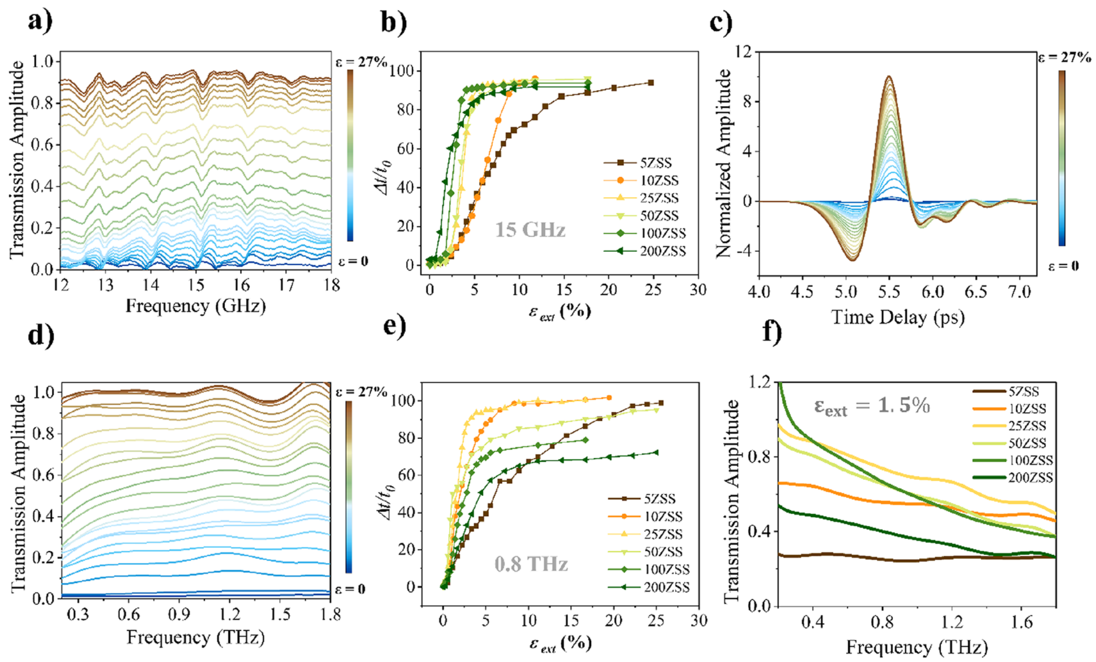

Figure 3. (a) Normalized transmission spectra for 5ZSS for various external strains in the microwave regime with a frequency range of 12 to 18 GHz. (b) Amplitude transmission change ($\Delta t/t_0$) at 15 GHz for different periodicities against different external strain (ε_{ext}). (c) Time traces of the transmitted terahertz electric field through 5ZSS for different applied strains and (d) resulting complex fast Fourier transform (FFT) in the frequency range of 0.2 to 1.8 THz. (e) Changing the amplitude of the transmission ($\Delta t/t_0$) for different periodicities against different external strains (ε_{ext}) at 0.8 THz. (f) Normalized amplitude for different periodicities with the external strain of ε_{ext} = 1.5% as a function of the frequency in the terahertz regime of 0.2 to 1.8 THz.

under 13% strain and the comparison with Au thin films under the same conditions are shown in Figure S2d−f in the Supporting Information. To showcase how uniform the whole sample is, diffraction patterns of the 50ZSS are shown in Figure 2f when illuminated by a helium−neon laser with a wavelength of 633 nm from a relaxed position up to an external strain of 20%. The combination of diffraction and interference effects on the light wave passing through the periodic slits produces a diffraction spectrum that appears in a symmetrical pattern on both sides of the zero-order direct light wave. Higher order diffracted wavefronts are tilted by an angle (θ) according to $\sin(\theta) = n\lambda/P$,[46] where λ is the wavelength of the wavefront, $P = p(1 + \varepsilon_{ext})$ is the periodicity of the slits, and n is an integer denoting the diffraction order.

To comprehensively investigate the optical and electrical properties of the whole ZSS samples, 2 cm × 2 cm, we perform broadband spectroscopy, including the terahertz and microwave regions and electrical measurements under various strain conditions. Transmission of ZSS with different periodicities is measured in the Ku-band (∼12−18 GHz) with a vector network analyzer (see Figure S3a, Supporting Information), while mechanical strain is applied using a computer- controlled piezoelectric translation stage with a 0.1 μm step (see Figure S3b, Supporting Information). Figure 3a shows the normalized transmission amplitude for 5ZSS under varying external strain. The maximum amplitude of over 90% for ε_{ext} > 20% implies that most gaps are open at large strains. Figure S4a displays transmission spectra for 100ZSS, showing a steeper rise at small strains. The sensitivity of the transmission amplitude ($\Delta t/t_0$), where $\Delta t = t - t_0$ and t_0 is the transmission at ε_{ext} = 0%, is plotted in Figure 3b at a frequency of 15 GHz for different periodicities against the external strain, consistent with the gap width dependence shown in Figure 2d. Figure S4b displays the hysteresis loops of 5ZSS during the cycles of stretching and relaxation at 15 GHz.

We also performed terahertz spectroscopy to investigate the transmission amplitude under an external strain. Figure 3c shows the transmission amplitude of 5ZSS in the time domain, normalized to the bare substrate, and Figure 3d shows the resulting complex fast Fourier transform (FFT) in the frequency range from 0.2 to 1.8 THz, under mechanical strain with a step size of 0.1%. Figure S4c (Supporting Information) shows the nonlinearity in the transmission spectra for the 100ZSS. As can be seen in Figure 3e, the transmission sensitivity ($\Delta t/t_0$) shows a different trend for different periodicities due to the comparability of the magnitude of the gap periodicity with the wavelength. It is shown that[47] for the gaps with large periodicity (larger than 25 μm in Figure 3f), due to the phenomenon of complete capacitive charging, where the induced charges accumulate specifically at the edge of the gap instead of dispersing away from it, the transmission increases with decreasing frequency and describes a $1/f$ dependence (as depicted in Figure S4d with $1/f$ fitting for 100ZSS in the Supporting Information). However, in the gaps with small periodicity (5ZSS), the slits share the accumulated charges due to the coupling of adjacent slits, and the transmission does not change at different frequencies (Figure S4d in the Supporting Information).

Furthermore, the performance of the ZSS is characterized by its relative resistance $\Delta R/R_0$, where $\Delta R = R - R_0$ and R_0 and R are the resistances before and after applying strain. The ZSS exhibits a linear current−voltage characteristic when subjected to different strains, indicating its proper ohmic behavior (Figure S5 for 5ZSS in the range of ε_{ext} = 0−18%, Supporting Information). The analysis of samples with different periodicities, in Figure 4a, indicates that the 5ZSS has a wide range

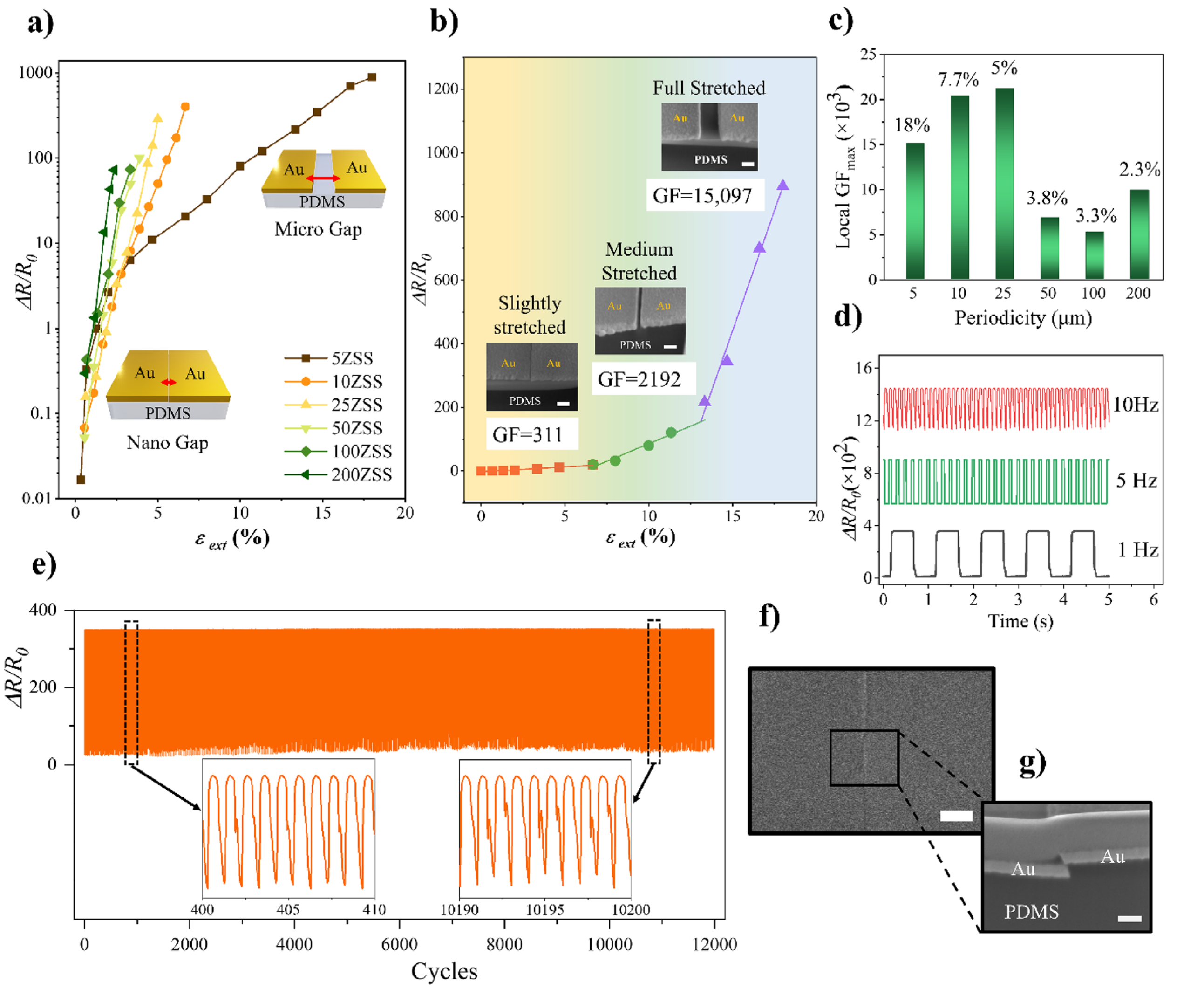

Figure 4. (a) Relative resistance-strain curve of different periodicities (the axis of $\Delta R/R_0$ is in log scale). (b) Sensing curves for 5ZSS and related local gauge factor at an indifferent strain range. The inset FE-SEM images show cross sections of the gap for 5ZSS in relaxed position, medium strain, and full stretched (scale bars are 500 nm). (c) Maximum gauge factor for samples with different periodicities. (d) Cyclic responses under external strain at modulation of 1 to 10 Hz. (e) 10 Hz durability test of 5ZSS for 12,000 cycles under 15% strain. Insets represent enlarged views of 10 cycles. FE-SEM images of (f) the top view and (g) the cross-sectional view of the 5ZSS gap after the fatigue test (scale bars 1 μm and 100 nm, respectively).

of sensitivities varying from $\Delta R/R_0 = 0.016$ to $\Delta R/R_0 = 800$ with strain changes from 0 to 18%. The external load increases the average relative resistance until two adjacent gold bars completely lose electrical contact, defining the end point of the strain range. The quantification of the sensitivity of a strain sensor is expressed by its gauge factor (GF) serving as a critical benchmark, particularly in the realm of high-sensitivity detection. Figure 4b shows the local gauge factor of the 5ZSS, defined as the slope of the relative resistance versus applied mechanical strain. The corresponding local gauge factors for 5ZSS are 311, 2192, and 15,097 for strain ranges of 0−5, 6−12, and 13−18%, respectively, demonstrating the versatility of the 5ZSS in all desired strain ranges compared to other metal-based strain sensors. The inset show FE-SEM images of the cross section of the gaps in slightly stretched, moderately stretched and fully opened state. The local gauge factor for different periodicities is displayed in Figure S6a−e (Supporting Information) and reveals the sensitivity at indifferent strain range. The comparison of the maximum gauge factor for different periodicities at their maximum strain limit is shown in Figure 4c. The highest gauge factor measured is 21,194 for 25ZSS at a strain range of 5%. Compared to other recently introduced metal-film strain sensors, our nano-to-micro strain sensors show superior performance in terms of sensitivity and gauge factor limit. We compared the sensing performance of our ZSS with other thin film strain sensors in Table S7 in the Supporting Information. We also measured the point gauge factors related to the sensitivity of the applied strain, defined as $GF = \Delta R/(\varepsilon_{ext}R_0)$ as shown in Figure S8 (Supporting Information). A gauge factor of over 6,038 is achieved for 10ZSS at 6.7% strain and 4,971 for 5ZSS at 18% strain before the samples completely lose the electrical connection. As a proof of the ultrahigh gauge factor of ZSS, we prepared a thin gold layer with the same thickness without pattern on the PDMS substrate. We used the same method for the binding of gold and PDMS: MPTMS molecules and generated cracks by initial stretching. We compared the performance of the thin film crack sensor by performing all experiments and measurements under the same conditions as those for the ZSS. Figure S9a in the Supporting Information

https://doi.org/10.1021/acsphotonics.4c00627
ACS Photonics 2024, 11, 3239−3249

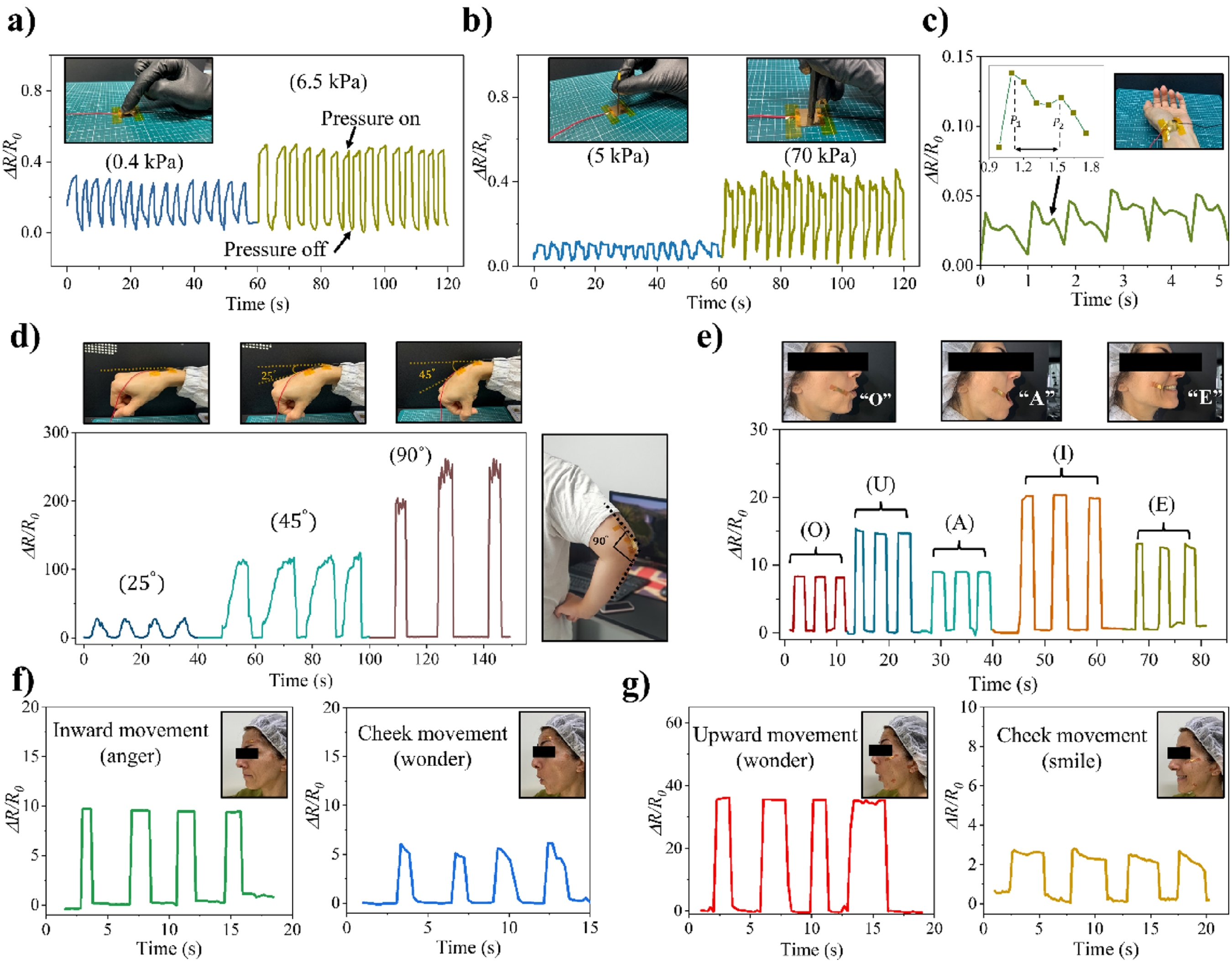

Figure 5. Detection of mechanical stimuli of the 5ZSS by (a) a slight finger touch with a pressure of 0.4 kPa and a hard pressing of the finger with 6.5 kPa and (b) pressing of hard objects with different surface areas (5 and 70 kPa). (c) Pulses of the radial artery with the sample attached to the wrist under normal conditions. The inset shows an enlarged single beat. (d) Detection of hand movements by attaching the sensors to the wrist with different angles of $\theta = 25°$ and $\theta = 45°$ and on the arm with $\theta = 90°$. (e) Images of the 5ZSS sensor attached to the corner of mouth and extracted strain signal during the vocalization of "O", "U", "A", "I" and "E". The response pattern of the 5ZSS is attached to (f) the upper edge of the eyebrows to recognize the inward and upward movement and (g) the cheeks for the expression of "wonder" and "smile".

compares the change in resistance of the sample with that of the 5ZSS and the thin film. The increase in resistance observed in the thin film when subjected to an external strain is much slower and with a gauge factor much lower than in 5ZSS (Figure S9b, Supporting Information). This phenomenon is attributed to the limited propagation of random microcracks along the surface of the thin film, which prevents their extensive opening and subsequent loss of electrical contact. In addition to the merit of broad sensing range with high gauge factor, these devices displayed significant durability throughout stretch and release tests, without any discernible degradation in performance. We analyzed the performance of our 5ZSS sensor at a frequency of 0.1 Hz at an applied strain of 0−15% in Figures S10a (Supporting Information). Figure 4d illustrates the frequency-dependent durability test of the 5ZSS sensor over a range of ultrafast modulation: 1, 5, and 10 Hz (and with smaller modulation depth for 20 Hz in Figure S10b in the Supporting Information). Importantly, the sensors consistently demonstrate a stable change in resistance regardless of the speed at which the external load is applied. This phenomenon is due to the strong bonding between the gold patterns and the PDMS, which guarantees the capability of our Zerogap strain sensor to withstand ultrahigh frequency modulations, a problem often faced by other strain sensors.[35] The remarkably fast response time of 11 ms for strain and 32 ms for recovery at 10 Hz is well suited for fast and accurate sensor measurements, as demonstrated by the change in resistance in Figure S10c,d in the Supporting Information for high (10 Hz) and low (0.1 Hz) modulation, respectively. In addition, the robustness of the sensor was thoroughly tested by showing negligible changes in the 10 Hz duration of the relative resistance response for 12,000 cycles in the 0−15% strain (Figure 4e) and the transmission response at 15 GHz for 25,000 cycles in the 0−20% strain (Figure S11, Supporting Information), showing identical peak patterns throughout. The FE-SEM images in top view (Figure 4f) and in the cross section (Figure 4g) show that the gaps are still well connected even after modulation, except that some parts show a slight overlap.

The stability of the strain sensors was evaluated under different conditions. As shown in Figure S12a,b (Supporting

https://doi.org/10.1021/acsphotonics.4c00627
ACS Photonics 2024, 11, 3239−3249

Information), the amplitude of microwave transmission of the 5ZSS sample remained stable as a function of applied strain over a period of 3 months, and the cyclic performance of the same sample showed constant stability over five months. We also investigated the performance of the sensor at different temperatures. As shown in Figures S11c,d (Supporting Information), the amplitude of microwave transmission at 15 GHz and the resistance of the 5ZSS, 10ZSS, and 25ZSS samples exhibited minimal variation from room temperature up to 60 °C, a range suitable for human body applications.

Wide Strain Range Applications of 5ZSS. Due to their exceptional adjustability, remarkable sensitivity, high strain capability, robust reliability, fast response times, and ease of fabrication, 5ZSS can be useful for an impressive array of applications, such as pressure sensing,[48−52] human−machine interfaces, and wearable technologies.[53−55] The "Experiments Section" describes in detail the specific techniques for attaching the sensors to human skin and the applied measurement methods. In the following, we focus on 5ZSS, which has the widest strain range before becoming insulating, owing to its small period. To demonstrate that the 5ZSS is suited for various low and high strain applications, we present the broad applicability of our sensor by recording the pressure strain and muscle movements of the human body. We have carried out tests with our ZSS as a wide-ranging pressure sensor. The strain signals recorded in real time show the cycles of strain and relief caused by the external pressure being turned on or off. The sensor consistently demonstrates an elastic and stable response across different pressure levels, including a slight finger touch at 0.4 kPa, finger pressure at 6.5 kPa, a narrow metal tip at 5 kPa, and a thick metal tip at 70 kPa each corresponding to different contact areas (see Figure 5a,b). As a very low strain application, we used the sensor to determine the radial artery pulse in a healthy volunteer by attaching the 5ZSS to the subject's wrist (Figure 5c). The blood pulse shows distinct systolic (P_1) and diastolic (P_2) peaks separated by 0.44s and an artery augmentation index $AIr = P_2/P_1 = 0.71$ within a healthy range for a 40-year-old.[56] The same 5ZSS can be employed to detect significant deformations during complicated human movements, such as muscle contractions, demonstrating the capability for large strain detection. The 5ZSS was attached to the wrist and reliably detected muscle movements that occurred during flexion. The sensor was subjected to tensile forces resulting in changes in resistance while the wrist was moved at different angles namely $\theta = 25°$ ($\Delta R/R_0 = 30$) and $\theta = 45°$ ($\Delta R/R_0 = 140$) (Figure 5d). It was also attached to the arm to detect $\theta = 90°$ movements, resulting in a deformation of $\Delta R/R_0 = 250$, demonstrating its ability to detect significant strains. The achieved sensitivity, spanning a remarkable range of $\Delta R/R_0$ from 0.05 to 250, surpasses the detection capabilities of traditional metal film strain sensors.[29,31,35,38]

Another application that requires high sensitivity for 5−10% of the strain range is the recording of signals from facial muscle movements. Earlier studies identified vowels that are essential units in speech and emotions such as smiling or anger, both through facial skin movements.[57−59] Our 5ZSS was applied to three areas of the face prone to experiencing most strain to measure vowel speech and facial expressions. The signals of the mouth were recorded in real time during the vocalization of "O", "U", "A", "I", and "E". Figure 5e shows the photograph of the subject's face with the sensors attached to the corner of the mouth and the stress signals during the utterance of the five different vowels, repeated three times for each vowel. The sensors were also attached to the upper edge of the eyebrows (Figure 5f) to detect the inward and upward movement of the eyebrow for "anger" and "wonder", respectively, and also on the cheeks (Figure 5g) for different expressions such as "wonder" and "smile". The sensitivity of 5ZSS allows distinguishing all the five vowels characteristic as well as characteristic facial expressions ranging $2 < \Delta R/R_0 < 40$, much better than conventional face recognition research limited a much smaller range, $\Delta R/R_0 < 10$.[33,54,59] Our strategy enables high performance designs and shows significant potential for practical applications in implantable soft electrodes, electrophysiological signals on the body surface, and smart sensors, paving the way for the advancement of future robotics.

■ CONCLUSIONS

We lithographically defined periodic Zerogaps on PDMS to be widened with strain Unlike random cracks in conventional metal thin films, our Zerogap strain sensor achieves substantial gap enlargement from the nanometer to micrometer scale with uniformity and repeatability. At the smallest periodicity of 5 μm, we observed a large gauge factor at the highest strain of 18%, demonstrating that we can cover a wider range of strains by simply reducing the periodicity. Our proposed strain sensor proposed here shows an impressive dynamic response in both speed and robustness in detecting fast modulations. This breakthrough in performance underlines the immense potential of our strain sensor for applications that require a wide range stretchability.

■ MATERIALS AND METHODS

Fabrication of ZSS. As shown schematically in Figure 1a, 120 nm vanadium as the first sacrificial layer, 3 nm titanium as the adhesion layer, and 50 nm gold are deposited on a 500 μm-thick silicone substrate using an e-beam evaporation system (KVE-E2000, Korea Vacuum Tech). To create a pattern on the Au layer, the process starts with coating AZ5214E photoresist with a spin coater at 4000 rpm for 60 s. Subsequently, the sample covered with a photomask with a 1:1 line/space stripe pattern (with different periodicity) is exposed to UV light at a wavelength of 365 nm in a mask aligner (MDA-400S, MIDAS). The desired photoresist pattern on the Au film is obtained after immersing the sample in AZ 300 MIF developer for 50 s. The underlying unprotected Au layers with the photoresist pattern are sequentially milled (KVET-IM4000, Korea Vacuum Tech) for 44 s using an argon ion beam with an incidence angle of 0°. After milling, a 3 nm thick titanium adhesion layer is applied, followed by a 50 nm-thick gold secondary layer. The final step is to immerse the sample in *N*-methyl-2-pyrrolidone (NMP) solvent at 90 °C for 3 h to remove the photoresist layer, resulting in the Zerogap structure. To generate MPTMS layers in liquid form, 100 μL of MPTMS was mixed with 100 mL ethanol to achieve the desired concentrations. Subsequently, the Si substrates with a Zerogap pattern were immersed in a Petri dish containing 10 mL of the MPTMS solution for 30 min and then dried with N2. The MPTMS treated sample was coated with a mixture of 1:10 PDMS base and curing agent at 500 rpm for 60 s and cured in an oven at 80° for 1 h. To achieve a desired thickness of 450 μm, the PDMS coating process is repeated twice. Finally, by immersing the sample in a chromium etchant, as it is compatible with Au, Ti, and PDMS, the vanadium etched

https://doi.org/10.1021/acsphotonics.4c00627
ACS Photonics 2024, 11, 3239−3249

away, resulting in the detachment of the Zerogap structure from the silicon substrate, allowing it to transfer onto the PDMS.

FE-SEM Measurement. The FE-SEM system (JSM-F100, Jeol), which is equipped with an in situ tensile stage, is used for direct observation of gap modulation under different strain conditions. The dual-beam FIB system (Helios Nano Lab 450) is used for the cross-sectional images of Zerogap.

Microwave Measurements. In the Ku-band frequency range (12−18 GHz), the Agilent Technologies E5063A ENA series network analyzer was used, employing a vertical waveguide setup (see Figure S3a in the Supporting Information) with the sample in the center. Microwave measurements were performed with a pair of open rectangular waveguides (62EWGN) connected to a network analyzer. The specific aperture size for the Ku-band was 15.80 × 7.90 mm to support the TE10 mode in this frequency range.

Preparation of the ZSS for Different Applications. A wafer-scale ZSS with a periodicity of 5 μm was fabricated on PDMS and cut with a paper cutter into different sizes such as (2 cm × 2 cm) and (1 cm × 2 cm) for different applications, and all were subjected to a 10-fold prestretching process before use.

Electrical Connection. The copper wires were attached to the sensor and connected to the source meter (Keithley 2450). The voltage of 1 V was used as the input signal, and the measured current was used as the output signal. The strain signals were analyzed in the form of resistance during stretching and releasing are studied in a real-time measurement in time length (number of time steps).

Pressure Sensing. The 2 cm by 2 cm size 5ZSS sensors were attached with Captone adhesive tape to the flat surface of the weighting machine with an accuracy of 0.01 g. We have measured the contact area of the pressure for the objects (here different sizes of screwdrivers as metallic objects and finger) and calculated the pressure = (force)/(contact area). The initial resistance of the sensor is approximately R_0 = 4 Ω and slightly varied for different samples. The maximum resistance experienced during the 70 kPa was 6.5 Ω and $\Delta R/R_0 \approx 0.5$, corresponding to the strain of 1%. The total free sensor length L (the length is not limited by the contact tapes) was 18 mm, so that the total maximum strain extension was $L_0 = L\varepsilon_{\text{ext}}/100 = 18 \times 1/100 = 0.18$ mm.

Radial Artery Pulse. To cover a larger area of the wrist to detect the pulse, the 2 cm by 2 cm 5ZSS sensor was attached to the skin of the wrist with adhesive strips. The initial resistance of the pulse was 23.4 Ω, and the maximum resistances for peaks $P1$ and $P2$ were 24.75 and 24.36 Ω, respectively.

Hand and Arm Motion with Different Angles. The 2 cm by 2 cm 5ZSS sensors were attached to the wrist and arm to record hand movements at different angles. For a movement of 25°, the initial resistance was R_0 = 12 Ω and reached the maximum resistance R = 346 Ω, $\Delta R/R_0 \approx 30$, corresponding to a stretch of 8% and a maximum total stretch of L_0 = 1.44 mm. A movement of 45° with R_0 = 20 Ω reaches the maximum resistance R = 2831 Ω, $\Delta R/R_0 \approx 140$, ε = 11%, and a maximum strain of L_0 = 2 mm. Finally, the movement of 90° with R_0 = 16 Ω reaches the maximum resistance R = 4010 Ω, $\Delta R/R_0 \approx 250$, ε = 15%, and the maximum strain of L_0 = 2.7 mm.

Face Gesture and Vowel Identification. The 1 cm by 2 cm 5ZSS were placed on the different parts of the face, especially on the areas that are subject to particularly high stress. In order to recognize the different pronunciation of vowels, the sensor was placed near the mouth and detect "O" with $\Delta R/R_0$= (1532 Ω − 166 Ω)/(166 Ω) = 8.2, "U" with $\Delta R/R_0$ = (782 Ω − 50 Ω)/(115 Ω) = 14.6, "A" with $\Delta R/R_0$= (1653 Ω − 166 Ω)/(166 Ω) = 8.9, "I" with $\Delta R/R_0$ = (2346 Ω − 110 Ω)/(110 Ω) = 20.3, and "E" with $\Delta R/R_0$= (1837 Ω − 130 Ω)/(130 Ω) = 13.1.

The sensor is placed on top of the eyebrow and detect "anger" and "wonder" expression by a resistance change in the range of $\Delta R/R_0$ = (1209 Ω − 115 Ω)/(115 Ω) = 9.5 and $\Delta R/R_0$ = (7300 Ω − 200 Ω)/(200 Ω) = 35.5, respectively. For cheek movements, the sensor detects the expression "wonder" and "smile" with $\Delta R/R_0$ = (500 Ω − 78 Ω)/(78 Ω) = 5.4 and $\Delta R/R_0$ =(160 Ω − 46 Ω)/(46 Ω) = 2.47, respectively.

ASSOCIATED CONTENT

Supporting Information

The Supporting Information is available free of charge at https://pubs.acs.org/doi/10.1021/acsphotonics.4c00627.

FE-SEM images and optical transmission of the entire stretching process; FE-SEM images of different periodicities and of the thin film; schematic diagram of the microwave transmission setup; microwave and terahertz transmission amplitude of the 5ZSS and 100ZSS; current−voltage curves of the 5ZSS; resistance sensing curves for different periodicities; comparison of the sensing performance of the ZSS with other thin film strain sensors; point gauge factor for different periodicities; the comparison of the sensitivity of ZSS and thin film; gap modulation of the 5ZSS and transmission durability test of the 5ZSS at 15 GHz; stability of the strain sensors under different conditions (PDF)

AUTHOR INFORMATION

Corresponding Authors

Bamadev Das − *Department of Physics, Ulsan National Institute of Science and Technology, Ulsan 44919, Republic of Korea; Quantum Photonics Institute, Ulsan National University of Science and Technology, Ulsan 44919, Republic of Korea*; Email: bamadevdas0@gmail.com

Dai Sik Kim − *Department of Physics, Ulsan National Institute of Science and Technology, Ulsan 44919, Republic of Korea; Quantum Photonics Institute and Center for Angstrom Scale Electromagnetism, Ulsan National University of Science and Technology, Ulsan 44919, Republic of Korea; Department of Physics and Astronomy, Seoul National University, Seoul 08826, Republic of Korea*; orcid.org/0000-0002-8950-1199; Email: daisikkim@unist.ac.kr

Authors

Mahsa Haddadi Moghaddam − *Department of Physics, Ulsan National Institute of Science and Technology, Ulsan 44919, Republic of Korea; Quantum Photonics Institute, Ulsan National University of Science and Technology, Ulsan 44919, Republic of Korea*

Daryll J. C Dalayoan − *Department of Physics, Ulsan National Institute of Science and Technology, Ulsan 44919, Republic of Korea; Quantum Photonics Institute, Ulsan National University of Science and Technology, Ulsan 44919, Republic of Korea*

Daehwan Park − *Department of Physics, Ulsan National Institute of Science and Technology, Ulsan 44919, Republic of*

Korea; Quantum Photonics Institute, Ulsan National University of Science and Technology, Ulsan 44919, Republic of Korea
Zhihao Wang − *Department of Physics, Ulsan National Institute of Science and Technology, Ulsan 44919, Republic of Korea; Quantum Photonics Institute, Ulsan National University of Science and Technology, Ulsan 44919, Republic of Korea*
Hwanhee Kim − *Department of Physics, Ulsan National Institute of Science and Technology, Ulsan 44919, Republic of Korea; Quantum Photonics Institute, Ulsan National University of Science and Technology, Ulsan 44919, Republic of Korea*
Sunghoon Im − *Department of Mechanical Engineering, Ajou University, Suwon 16499, Republic of Korea*
Kyungbin Ji − *Department of Mechanical Engineering, Ajou University, Suwon 16499, Republic of Korea*
Daeshik Kang − *Department of Mechanical Engineering, Ajou University, Suwon 16499, Republic of Korea*

Complete contact information is available at:
https://pubs.acs.org/10.1021/acsphotonics.4c00627

Author Contributions

M.H.M. fabricated the samples, designed, and performed the experiments and data analysis, and wrote the manuscript; B.D. designed the experiments; Z.W., D.D., D.P., H.K., S.M., and K.J. helped the measurements; D.K., reviewed and edited the manuscript; D.S.K. conceived the idea, led the work, reviewed, edited, and supervised this work.

Notes

The authors declare no competing financial interest.

The authors cite the preprint version of the work in this manuscript. Moghaddam, M. H.; Wang, Z.; Dalayoan, D. J.; Park, D.; Kim, H.; Im, S.; Ji, K.; Kang, D.; Das, B.; Kim, D. S. Lithographically Defined Zerogap Strain Sensors. *arXiv preprint arXiv:2403.08288* 2024, DOI: 10.48550/arXiv.2403.08288.

■ ACKNOWLEDGMENTS

This work was supported by the National Research Foundation of Korea (NRF) grant funded by the Korean government (MSIT: NRF-2015R1A3A2031768), the National R&D Program through the National Research Foundation of Korea (NRF) funded by Ministry of Science and ICT (2022M3H4A1A04096465), the Basic Science Research Program through the National Research Foundation of Korea (NRF) funded by the Ministry of Education (NRF-2022R1I1A1A01073838), and the MSIT (Ministry of Science and ICT), Korea, under the ITRC (Information Technology Research Center) support program (IITP-2023-RS-2023-00259676) supervised by the IITP (Institute for Information & Communications Technology Planning & Evaluation). The authors would also like to express their sincere gratitude to Dr. S Jagan Mohan Rao for his invaluable help in the preparation of the samples used in this study.

■ REFERENCES

(1) Chou, H.-H.; Nguyen, A.; Chortos, A.; To, J. W. F.; Lu, C.; Mei, J.; Kurosawa, T.; Bae, W.-G.; Tok, J. B. H.; Bao, Z. A chameleon-inspired stretchable electronic skin with interactive colour changing controlled by tactile sensing. *Nat. Commun.* **2015**, *6* (1), 8011.

(2) Li, L.; Xiang, H.; Xiong, Y.; Zhao, H.; Bai, Y.; Wang, S.; Sun, F.; Hao, M.; Liu, L.; Li, T.; et al. Ultrastretchable Fiber Sensor with High Sensitivity in Whole Workable Range for Wearable Electronics and Implantable Medicine. *Advanced Science* **2018**, *5* (9), 1800558.

(3) Li, S.; Liu, G.; Li, R.; Li, Q.; Zhao, Y.; Huang, M.; Zhang, M.; Yin, S.; Zhou, Y.; Tang, H.; et al. Contact-Resistance-Free Stretchable Strain Sensors with High Repeatability and Linearity. *ACS Nano* **2022**, *16* (1), 541−553.

(4) Liao, X.; Liao, Q.; Yan, X.; Liang, Q.; Si, H.; Li, M.; Wu, H.; Cao, S.; Zhang, Y. Flexible and Highly Sensitive Strain Sensors Fabricated by Pencil Drawn for Wearable Monitor. *Adv. Funct. Mater.* **2015**, *25* (16), 2395−2401.

(5) Tricoli, A.; Nasiri, N.; De, S. Wearable and Miniaturized Sensor Technologies for Personalized and Preventive Medicine. *Adv. Funct. Mater.* **2017**, *27* (15), 1605271.

(6) Zhou, J.; Yu, H.; Xu, X.; Han, F.; Lubineau, G. Ultrasensitive, Stretchable Strain Sensors Based on Fragmented Carbon Nanotube Papers. *ACS Appl. Mater. Interfaces* **2017**, *9* (5), 4835−4842.

(7) Araromi, O. A.; Graule, M. A.; Dorsey, K. L.; Castellanos, S.; Foster, J. R.; Hsu, W.-H.; Passy, A. E.; Vlassak, J. J.; Weaver, J. C.; Walsh, C. J.; et al. Ultra-sensitive and resilient compliant strain gauges for soft machines. *Nature* **2020**, *587* (7833), 219−224.

(8) Kim, J.; Lee, G.; Heimgartner, R.; Arumukhom Revi, D.; Karavas, N.; Nathanson, D.; Galiana, I.; Eckert-Erdheim, A.; Murphy, P.; Perry, D.; et al. Reducing the metabolic rate of walking and running with a versatile, portable exosuit. *Science* **2019**, *365* (6454), 668−672. From NLM.

(9) Tolvanen, J.; Hannu, J.; Jantunen, H. Stretchable and Washable Strain Sensor Based on Cracking Structure for Human Motion Monitoring. *Sci. Rep.* **2018**, *8* (1), 13241.

(10) Xu, J.; Zhang, Z.; Gan, S.; Gao, H.; Kong, H.; Song, Z.; Ge, X.; Bao, Y.; Niu, L. Highly Stretchable Fiber-Based Potentiometric Ion Sensors for Multichannel Real-Time Analysis of Human Sweat. *ACS Sensors* **2020**, *5* (9), 2834−2842.

(11) You, I.; Kim, B.; Park, J.; Koh, K.; Shin, S.; Jung, S.; Jeong, U. Stretchable E-Skin Apexcardiogram Sensor. *Adv. Mater.* **2016**, *28* (30), 6359−6364.

(12) Liu, Z.; Qi, D.; Guo, P.; Liu, Y.; Zhu, B.; Yang, H.; Liu, Y.; Li, B.; Zhang, C.; Yu, J.; et al. Thickness-Gradient Films for High Gauge Factor Stretchable Strain Sensors. *Adv. Mater.* **2015**, *27* (40), 6230−6237.

(13) Tang, Z.; Jia, S.; Shi, X.; Li, B.; Zhou, C. Coaxial Printing of Silicone Elastomer Composite Fibers for Stretchable and Wearable Piezoresistive Sensors. *Polymers* **2019**, *11* (4), 666.

(14) Xiang, D.; Zhang, X.; Harkin-Jones, E.; Zhu, W.; Zhou, Z.; Shen, Y.; Li, Y.; Zhao, C.; Wang, P. Synergistic effects of hybrid conductive nanofillers on the performance of 3D printed highly elastic strain sensors. *Composites Part A: Applied Science and Manufacturing* **2020**, *129*, No. 105730.

(15) Zhou, Y.; Zhan, P.; Ren, M.; Zheng, G.; Dai, K.; Mi, L.; Liu, C.; Shen, C. Significant Stretchability Enhancement of a Crack-Based Strain Sensor Combined with High Sensitivity and Superior Durability for Motion Monitoring. *ACS Appl. Mater. Interfaces* **2019**, *11* (7), 7405−7414.

(16) Han, F.; Li, J.; Zhao, S.; Zhang, Y.; Huang, W.; Zhang, G.; Sun, R.; Wong, C.-P. A crack-based nickel@graphene-wrapped polyurethane sponge ternary hybrid obtained by electrodeposition for highly sensitive wearable strain sensors. *Journal of Materials Chemistry C* **2017**, *5* (39), 10167−10175.

(17) Liu, Q.; Chen, J.; Li, Y.; Shi, G. High-Performance Strain Sensors with Fish-Scale-Like Graphene-Sensing Layers for Full-Range Detection of Human Motions. *ACS Nano* **2016**, *10* (8), 7901−7906. From NLM.

(18) Wang, Z.; Li, P.; Song, R.; Qian, W.; Zhou, H.; Wang, Q.; Wang, Y.; Zeng, X.; Ren, L.; Yan, S.; et al. High conductive graphene assembled films with porous micro-structure for freestanding and ultra-low power strain sensors. *Science Bulletin* **2020**, *65* (16), 1363−1370.

(19) Zhao, J.; He, C.; Yang, R.; Shi, Z.; Cheng, M.; Yang, W.; Xie, G.; Wang, D.; Shi, D.; Zhang, G. Ultra-sensitive strain sensors based

on piezoresistive nanographene films. *Appl. Phys. Lett.* **2012**, *101*, No. 063112.
(20) Zhao, J.; Wang, G.; Yang, R.; Lu, X.; Cheng, M.; He, C.; Xie, G.; Meng, J.; Shi, D.; Zhang, G. Tunable Piezoresistivity of Nanographene Films for Strain Sensing. *ACS Nano* **2015**, *9* (2), 1622−1629.
(21) Liang, F.-C.; Ku, H.-J.; Cho, C.-J.; Chen, W.-C.; Lee, W.-Y.; Chen, W.-C.; Rwei, S.-P.; Borsali, R.; Kuo, C.-C. An intrinsically stretchable and ultrasensitive nanofiber-based resistive pressure sensor for wearable electronics. *Journal of Materials Chemistry C* **2020**, *8* (16), 5361−5369.
(22) Veeramuthu, L.; Cho, C. J.; Liang, F. C.; Venkatesan, M.; Kumar G, R.; Hsu, H. Y.; Chung, R. J.; Lee, C. H.; Lee, W. Y.; Kuo, C. C. Human Skin-Inspired Electrospun Patterned Robust Strain-Insensitive Pressure Sensors and Wearable Flexible Light-Emitting Diodes. *ACS Appl. Mater. Interfaces* **2022**, *14* (26), 30160−30173.
(23) Veeramuthu, L.; Cho, C. J.; Venkatesan, M.; Kumar. G, R.; Hsu, H. Y.; Zhuo, B. X.; Kau, L. J.; Chung, M. A.; Lee, W. Y.; Kuo, C. C. Muscle fibers inspired electrospun nanostructures reinforced conductive fibers for smart wearable optoelectronics and energy generators. *Nano Energy* **2022**, *101*, No. 107592.
(24) Venkatesan, M.; Chandrasekar, J.; Liang, F.-C.; Lin, W.-C.; Chen, W.-C.; Cho, C.-J.; Chen, Y.-T.; Lee, W.-Y.; Su, C.; Zhou, Y.; et al. Surface-enhanced fully nanofiber-based self-cleanable ultraviolet resistive triboelectric energy harvester for wearable smart garments. *Nano Energy* **2023**, *113*, No. 108556.
(25) Venkatesan, M.; Veeramuthu, L.; Liang, F.-C.; Chen, W.-C.; Cho, C.-J.; Chen, C.-W.; Chen, J.-Y.; Yan, Y.; Chang, S.-H.; Kuo, C.-C. Evolution of electrospun nanofibers fluorescent and colorimetric sensors for environmental toxicants, pH, temperature, and cancer cells − A review with insights on applications. *Chemical Engineering Journal* **2020**, *397*, No. 125431.
(26) Liu, G. S.; Yang, F.; Xu, J.; Kong, Y.; Zheng, H.; Chen, L.; Chen, Y.; Wu, M. X.; Yang, B. R.; Luo, Y.; et al. Ultrasonically Patterning Silver Nanowire-Acrylate Composite for Highly Sensitive and Transparent Strain Sensors Based on Parallel Cracks. *ACS Appl. Mater. Interfaces* **2020**, *12* (42), 47729−47738. From NLM.
(27) Zhao, W.; Luo, J.; Shan, S.; Lombardi, J. P.; Xu, Y.; Cartwright, K.; Lu, S.; Poliks, M.; Zhong, C.-J. Nanoparticle-Structured Highly Sensitive and Anisotropic Gauge Sensors. *Small* **2015**, *11* (35), 4509−4516.
(28) Zhong, W.; Liu, C.; Xiang, C.; Jin, Y.; Li, M.; Liu, K.; Liu, Q.; Wang, Y.; Sun, G.; Wang, D. Continuously Producible Ultrasensitive Wearable Strain Sensor Assembled with Three-Dimensional Interpenetrating Ag Nanowires/Polyolefin Elastomer Nanofibrous Composite Yarn. *ACS Appl. Mater. Interfaces* **2017**, *9* (48), 42058−42066.
(29) Zhu, J.; Wu, X.; Jan, J.; Du, S.; Evans, J.; Arias, A. C. Tuning Strain Sensor Performance via Programmed Thin-Film Crack Evolution. *ACS Appl. Mater. Interfaces* **2021**, *13* (32), 38105−38113.
(30) Zhu, T.; Wu, K.; Xia, Y.; Yang, C.; Chen, J.; Wang, Y.; Zhang, J.; Pu, X.; Liu, G.; Sun, J. Topological Gradients for Metal Film-Based Strain Sensors. *Nano Lett.* **2022**, *22* (16), 6637−6646.
(31) Yang, T.; Li, X.; Jiang, X.; Lin, S.; Lao, J.; Shi, J.; Zhen, Z.; Li, Z.; Zhu, H. Structural engineering of gold thin films with channel cracks for ultrasensitive strain sensing. *Materials Horizons* **2016**, *3* (3), 248−255.
(32) Meng, X.; Sun, T.; Liu, L.; Zhang, C.; Zhao, H.; Wang, D.; Zhang, J.; Niu, S.; Han, Z.; Ren, L. Flexible Equivalent Strain Sensor with Ordered Concentric Circular Curved Cracks Inspired by Scorpion. *ACS Appl. Mater. Interfaces* **2022**, *14* (25), 29441−29450. From NLM.
(33) Lee, W. S.; Kim, D.; Park, B.; Joh, H.; Woo, H. K.; Hong, Y.-K.; Kim, T.-i.; Ha, D.-H.; Oh, S. J. Multiaxial and Transparent Strain Sensors Based on Synergetically Reinforced and Orthogonally Cracked Hetero-Nanocrystal Solids. *Adv. Funct. Mater.* **2019**, *29* (4), 1806714.
(34) Lee, T.; Choi, Y. W.; Lee, G.; Kim, S. M.; Kang, D.; Choi, M. Crack-based strain sensor with diverse metal films by inserting an inter-layer. *RSC Adv.* **2017**, *7* (55), 34810−34815.
(35) Kang, D.; Pikhitsa, P. V.; Choi, Y. W.; Lee, C.; Shin, S. S.; Piao, L.; Park, B.; Suh, K. Y.; Kim, T. I.; Choi, M. Ultrasensitive mechanical crack-based sensor inspired by the spider sensory system. *Nature* **2014**, *516* (7530), 222−226. From NLM.
(36) Zhou, R.; Zhang, Y.; Xu, F.; Song, Z.; Huang, J.; Li, Z.; Gao, C.; He, J.; Gao, W.; Pan, C. Hierarchical Synergistic Structure for High Resolution Strain Sensor with Wide Working Range. *Small* **2023**, *19* (34), 2301544. (acccessed 2024/05/22).
(37) Zhu, D.; Duan, S.; Liu, J.; Diao, S.; Hong, J.; Xiang, S.; Wei, X.; Xiao, P.; Xia, J.; Lei, W.; et al. A double-crack structure for bionic wearable strain sensors with ultra-high sensitivity and a wide sensing range. *Nanoscale* **2024**, *16* (10), 5409−5420.
(38) Liu, J.; Guo, H.; Li, M.; Zhang, C.; Chu, Y.; Che, L.; Zhang, Z.; Li, R.; Sun, J.; Lu, Y. Photolithography-assisted precise patterning of nanocracks for ultrasensitive strain sensors. *Journal of Materials Chemistry A* **2021**, *9* (7), 4262−4272.
(39) Ye, J.; Yang, T.; Zhang, Y.; Lin, L. Single-Crack-Activated Ultrasensitive Impedance Strain Sensor. *Advanced Materials Interfaces* **2018**, *5* (19), 1800616.
(40) Seghir, R.; Arscott, S. Controlled mud-crack patterning and self-organized cracking of polydimethylsiloxane elastomer surfaces. *Sci. Rep.* **2015**, *5* (1), 14787.
(41) Nam, K. H.; Park, I. H.; Ko, S. H. Patterning by controlled cracking. *Nature* **2012**, *485* (7397), 221−224. From NLM.
(42) Das, B.; Yun, H. S.; Park, N.; Jeong, J.; Kim, D. A Transformative Metasurface Based on Zerogap Embedded Template. *Advanced Optical Materials* **2021**, *9*, 2002164.
(43) Kim, S.; Das, B.; Ji, K. H.; Moghaddam, M. H.; Chen, C.; Cha, J.; Namgung, S.; Lee, D.; Kim, D.-S. Defining the zerogap: cracking along the photolithographically defined Au−Cu−Au lines with sub-nanometer precision. *Nanophotonics* **2023**, *12* (8), 1481−1489. (acccessed 2024−01−29).
(44) Filiatrault, H. L.; Carmichael, R. S.; Boutette, R. A.; Carmichael, T. B. A Self-Assembled, Low-Cost, Microstructured Layer for Extremely Stretchable Gold Films. *ACS Appl. Mater. Interfaces* **2015**, *7* (37), 20745−20752.
(45) Liu, Z.; Wang, H.; Huang, P.; Huang, J.; Zhang, Y.; Wang, Y.; Yu, M.; Chen, S.; Qi, D.; Wang, T.; et al. Highly Stable and Stretchable Conductive Films through Thermal-Radiation-Assisted Metal Encapsulation. *Adv. Mater.* **2019**, *31* (35), 1901360. (acccessed 2023/12/21).
(46) Hecht, E. *Optics*; Pearson, 2012.
(47) Bahk, Y.-M.; Han, S.; Rhie, J.; Park, J.; Jeon, H.; Park, N.; Kim, D.-S. Ultimate terahertz field enhancement of single nanoslits. *Phys. Rev. B* **2017**, *95* (7), No. 075424.
(48) Lipomi, D. J.; Vosgueritchian, M.; Tee, B. C.; Hellstrom, S. L.; Lee, J. A.; Fox, C. H.; Bao, Z. Skin-like pressure and strain sensors based on transparent elastic films of carbon nanotubes. *Nat. Nanotechnol* **2011**, *6* (12), 788−792. From NLM.
(49) Tian, K.; Sui, G.; Yang, P.; Deng, H.; Fu, Q. Ultrasensitive Thin-Film Pressure Sensors with a Broad Dynamic Response Range and Excellent Versatility Toward Pressure, Vibration, Bending, and Temperature. *ACS Appl. Mater. Interfaces* **2020**, *12* (18), 20998−21008. From NLM.
(50) Tao, L.-Q.; Zhang, K.-N.; Tian, H.; Liu, Y.; Wang, D.-Y.; Chen, Y.-Q.; Yang, Y.; Ren, T.-L. Graphene-Paper Pressure Sensor for Detecting Human Motions. *ACS Nano* **2017**, *11* (9), 8790−8795.
(51) Almassri, A. M.; Wan Hasan, W. Z.; Ahmad, S. A.; Ishak, A. J.; Ghazali, A. M.; Talib, D. N.; Wada, C. Pressure Sensor: State of the Art, Design, and Application for Robotic Hand. *J. Sens.* **2015**, *2015* (1), No. 846487.
(52) Tian, H.; Shu, Y.; Wang, X. F.; Mohammad, M. A.; Bie, Z.; Xie, Q. Y.; Li, C.; Mi, W. T.; Yang, Y.; Ren, T. L. A graphene-based resistive pressure sensor with record-high sensitivity in a wide pressure range. *Sci. Rep* **2015**, *5*, 8603. From NLM.
(53) Wang, M.; Yan, Z.; Wang, T.; Cai, P.; Gao, S.; Zeng, Y.; Wan, C.; Wang, H.; Pan, L.; Yu, J.; et al. Gesture recognition using a bioinspired learning architecture that integrates visual data with

somatosensory data from stretchable sensors. *Nat. Electron.* **2020**, *3*, 563.
(54) He, Y.; Wu, D.; Zhou, M.; Zheng, Y.; Wang, T.; Lu, C.; Zhang, L.; Liu, H.; Liu, C. Wearable Strain Sensors Based on a Porous Polydimethylsiloxane Hybrid with Carbon Nanotubes and Graphene. *ACS Appl. Mater. Interfaces* **2021**, *13* (13), 15572−15583.
(55) Araromi, O. A.; Graule, M. A.; Dorsey, K. L.; Castellanos, S.; Foster, J. R.; Hsu, W. H.; Passy, A. E.; Vlassak, J. J.; Weaver, J. C.; Walsh, C. J.; et al. Ultra-sensitive and resilient compliant strain gauges for soft machines. *Nature* **2020**, *587* (7833), 219−224. From NLM.
(56) Nichols, W. W. Clinical measurement of arterial stiffness obtained from noninvasive pressure waveforms. *Am. J. Hypertens.* **2005**, *18* (1 Pt 2), 3S−10S. From NLM.
(57) Yoo, H.; Kim, E.; Chung, J. W.; Cho, H.; Jeong, S.; Kim, H.; Jang, D.; Kim, H.; Yoon, J.; Lee, G. H.; et al. Silent Speech Recognition with Strain Sensors and Deep Learning Analysis of Directional Facial Muscle Movement. *ACS Appl. Mater. Interfaces* **2022**, *14* (48), 54157−54169. From NLM.
(58) Kim, T.; Shin, Y.; Kang, K.; Kim, K.; Kim, G.; Byeon, Y.; Kim, H.; Gao, Y.; Lee, J. R.; Son, G.; et al. Ultrathin crystalline-silicon-based strain gauges with deep learning algorithms for silent speech interfaces. *Nat. Commun.* **2022**, *13* (1), 5815.
(59) Cheng, L.; Ruan, D.; He, Y.; Yang, J.; Qian, W.; Zhu, L.; Zhu, P.; Wu, H.; Liu, A. A highly stretchable and sensitive strain sensor for lip-reading extraction and speech recognition. *Journal of Materials Chemistry C* **2023**, *11* (25), 8413−8422.

https://doi.org/10.1021/acsphotonics.4c00627
ACS Photonics 2024, 11, 3239−3249